Carbon Dusting Mechanisms and Countermeasures

Matthias Dechent
Production Manager Electrolysis
TRIMET Aluminium SE, Voerde, Germany
matthias.dechent@trimet.de
https://doi.org/10.71659/icsoba2024-al040

Abstract

Carbon anodes are an integral component of the molten salt electrolysis for primary aluminium production. Raw materials for anode production are suffering a reduction in quality and the aluminium world faces competition from lithium-ion batteries. The knowledge and improved process control in anode manufacturing has increased, where now anodes are manufactured to a better quality than 40 years ago. Despite the improved quality of the anodes, the problem of carbon particles mixed into the electrolyte (also known as carbon dust) is still prevalent. The usual recommendation in operations in smelters is: "Get better anodes and the problem will take care of itself". This summary of PhD thesis aims to investigate carbon particles and their distribution in industrial electrolyte taken from cells in the TRIMET Hamburg smelter.

An electrolyte sample containing carbon particles was analysed using STEM-EDS. The particles have an increased sodium content on the surface, which indicates sodium intercalation. Analysing the results of the industrial sampling at 600 positions, cells did not reveal fundamental patterns of carbon distribution. Modelling using PCR was able to explain a maximum of 19.1 % variance in the average carbon concentration. No mechanism was found to be acting on the distribution – in contrasts to other components in the electrolyte.

The analysis of frozen electrolyte samples taken under newly changed anodes within eight hours shows layered structures of the frozen bath. Many of the samples contained carbon particles. The size of the particles depended on whether the anode change was carried out using a scoop to clean the surface of the open electrolyte. Fine carbon particles remained in most cases. The formation of spikes, which damage the process, could not be detected in any of the anode changes observed within the first eight hours.

Overall, the methods and analysis conducted in this study did not show common particle patterns. The carbon particle distribution can be random.

Keywords: Carbon dust, Microstructure, Carbon distribution in bath, PCR, STEM-EDS.

1. Introduction

The use of carbon anodes in the primary production of aluminium has been the status quo since the inception of the process itself. While the overall demand for aluminium is growing, the primary production is hampered by its direct and indirect CO_2 emissions, which are contrasting the use in the green transformation. While today the CO_2 scope 2 footprint of aluminium ranges between four and 16.5 t CO_2-e/t Al [1-3], the reduction with green energy will only go so far. In the end, the process of carbon oxidation in the production is still relevant, until the inert anode is successfully integrated on a large scale, or an alternative process has been industrialized. However, the oxidation and consumption of carbon is both intentional and - due to side reactions - unintentional.

1.1 Carbon Reactivity in Electrolysis Cells

Carbon particles can be found in the electrolyte. The definition of carbon dust was published by the author elsewhere [4]:

"Carbon dust refers to small carbon particles, which are located in the electrolyte of an aluminium reduction cell [5-7]. Older sources refer to carbon slough [8] or carbon foam [9], which refers to a mixture of carbon particles of various sizes within the electrolyte in an aluminium reduction cell."

Carbon dusting can be considered unintentional carbon consumption. It occurs due to various processes within the electrolysis process. The main ones are the reactivity of anodes with air or CO_2. Figure 1 shows an anode with the temperature zones and the areas of air and CO_2 reactivity.

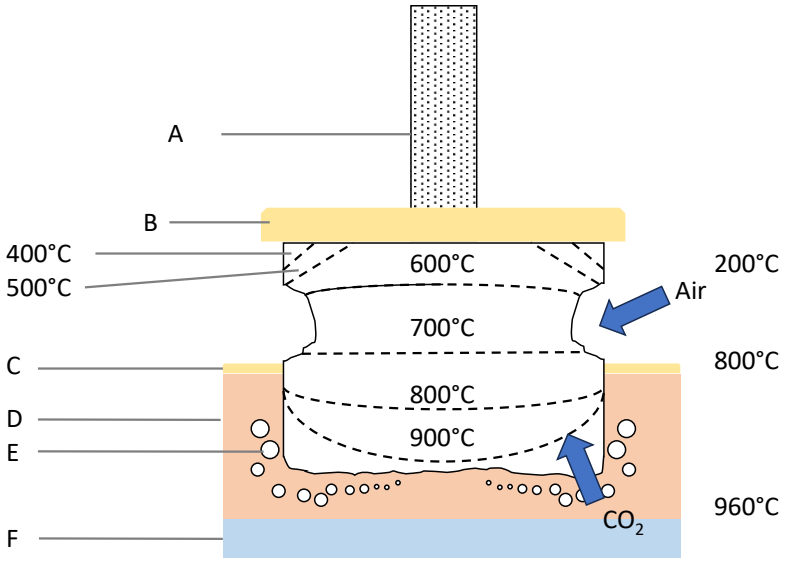

Figure 1. Anode sketch with zones of O_2 and CO_2 reactivity. The temperature scale shows the increasing temperature of the anode from top to bottom. Bottom surface profile of anode is exaggerated. With a temperature between 550 – 600 °C air reactivity starts, when air is available (arrow left of the word Air). This part can be, depending on the cell design, operation and time in the anode cycle, above anode cover material, which is supposed to seal the anode from air access. A: anode rod, B: Anode Cover Material, C: Bath Crust, D: Electrolyte, E: CO_2 bubbles, F: Aluminium. Recreated from Fischer and Perruchoud [10].

The rate and amount of CO_2 reactivity are temperature dependent and influenced by the anode properties [10-11]. Polished butts (used anodes) cores were investigated at 10x magnification. Sadler et al. showed a higher rate of sub-surface carboxy attack on the sides of anodes, when compared to the working surface [12]. Engvoll et al. supported the finding by analysing samples over the height of an anode after use [13]. Both groups stated that CO_2 can move through porosity for up to 50 mm and oxidize the binder phase of the anode. These "pre-reacted" parts are consumed on the working surface, as protruding particles are consumed preferential [12-13]. The importance of porosity as an indicator for anode quality was highlighted by Galisiu et al., who proposed the ratio of large porosity (pore diameter > 7.5 µm) by total porosity as a proxy for anode quality. There was a strong correlation between the porosity ratio and anode performance [14].

The anode working bottom surface temperature is expected to be close to the cell temperature. The anode lateral and top surface temperatures vary with anode geometry and thermal conductivity of the anode [15]. These temperatures are also dependent on the thermal conductivity of the yoke assembly and the internal heat generation in the anode [16]. The top temperature of an anode reaches 550 °C after 42.5 hours according to [15]. Fischer and Perruchoud stated that the airburn rate at that temperature can reach 1 mm/ hour and for temperature increases of 30 °C, the rate doubles [10]. Engvoll found that gasification can occur as deep as 40 mm below the anodes top surface and is therefore invisible for any operator [13].

Preventive measures to reduce CO_2 reactivity are rather limited, however airburn can be effectively prevented with anode cover material and anode dressing practice [17]. Since the 1990s, anodes are covered with a mixture of alumina and frozen electrolyte, which necessitated an increase of base voltage due to a higher heat dissipation, when compared to pure alumina [18], [19]. Bird et al. found 40 to 50 mm of anode cover material to be sufficient to prevent access of ambient air at the anode [11]. The composition of anode cover material changes over the anode cycle. At the beginning and at 520 °C, coarse material can wick heat away more efficiently than fine material [20]. With an increase of temperature, components like chiolite start to melt [21]. At the end of the anode cycle, the cover material closest to the anode top surface contains mostly alumina [22].

Lhussier et al. and others proposed the use of under-calcined coke to reduce the reactivity gradient within an anode, as the coke would be co-calcined with the binder matrix. The co-calcining would however necessitate a change in the baking furnace process to reach higher temperatures for longer durations, hence a higher energy consumption and a lower throughput in the baking furnace [23-24].

The standardized tests for air and carboxy reactivity include three quantitative figures, which are a percentage of the original weight: residue, which is the residual sample after tumbling; dust, which is the part of the material which has been tumbled out; and loss, which is the amount of actual oxidation, and therefore carbon which has been removed by gasification (ISO 12988-1 and ISO 12989-1). The process can take place during normal electrolysis. However, we can only find the residue in different particle sizes or the dust in our electrolyte, while the loss has evaporated as gas.

Sodium inclusions strongly correlate with high air and CO_2 reactivity [25]. Hume et al. investigated the influence of sodium levels in butts. The study showed that an increase of 1.5 % Na could reduce the CO_2 reactivity residue (CRR) by 19 %. According to the study's findings, sulphur creates sulphur sodium complexes, which hinder the diffusion of sodium in the anode structure [26].

According to Perruchoud et al., carbon dust generation per tonne can be assumed at 5 kg/t Al [27]. The skimmings contain between five and 32 % carbon, amassing 20 to 50 kg skimmings per tonne of aluminium [28-29]. For the Hamburg smelter, the amount of skimmings disposed between 2020 to 2022 was between 3.44 and 4.52 kg/t Al at cost between 390.69 and 438.30 €/ t carbon dust skimming to remove carbon material from the internal recycling loop. As some of the carbon dust is recycled through anode cover recycling, the actual amount is to be expected higher.

1.2 Electrolyte Inclusions and Inhomogeneities

Inhomogeneities in the electrolyte composition within a single electrolysis cell are in stark contrast to the assumed control mechanism of one specific resistance (R/mm) per cell, which is used for process control [30]. The resistance is used both for beam movements and decision

making in alumina feeding [31]. This chapter will only include alumina and carbon inhomogeneities within the electrolyte.

1.2.1 Alumina Distribution

The field of alumina (Al_2O_3) distribution has been the center of several investigations. Tessier et al. sampled on the AP 30 technology 12 positions on the side channel to find an average concentration between 1.89 and 3.94 % Al_2O_3 on three cells. Individual ranges in the cell were between 1.6 and 2.8 % Al_2O_3, significantly higher than the average range. Bazhin et al samples cells in two cell technologies. The range found for one technology was between 2.9 and 4.19 in horizontal variation. They found even higher gradients for vertical direction [32]. Lavoie and Taylor analysed the local and spatial alumina distribution due to feeding rates. Their results showed large concentration gradients, which can lead to local anode effects [33].

Dando et al. reported the formation of alumina rafts, which are formed from alumina freezing the electrolyte surface during feeding. The rafts are favoured by the use of clumpy alumina [34]. These rafts slow according to Gylver et al. the dissolution rate of alumina, as the rafts need to remelt. Only then alumina can be dissolved and transported throughout the cell [35]. Bojarevics and Dupuis named raft formation as a key issue for inhomogeneous alumina concentration [36]. In a model they showed that very different alumina concentrations were calculated within the cells after eight feed cycles. The adaptation of feeding positions could produce a more uniform alumina concentration [37]. However, the adaptation this would require a cell redesign. A redesign study was conducted by Severo et al. They simulated the effect of constrictions and changes in feeder position in order to achieve an improved alumina and bath flow. The simulation was verified in actual cells and succeeded [38].

1.2.2 Carbon Particles as Inhomogeneities

The difference between carbon and alumina is the mechanism of addition. While alumina is fed in controlled doses, carbon particles form within the cell and are transported by distribution forces within the cell. A number of processes both inside and outside the aluminium electrolysis cell are responsible for carbon dust formation. Grjotheim et al. highlighted the points 1 – 4, while Fischer et al. and Sadler with Welch added the remaining points [39-41]:

1. Aluminium oxidation by CO or CO_2 (back reaction) forming elemental carbon.
2. Selective oxidation of the anode on the sides and in the slots [23].
3. Erosion and cathodic dissolution of ramming paste, carbon lining and cathodes, formation of aluminium carbide [42-43].
4. In Vertical Stud Söderberg: pitch leaking through cracks or stud holes in the bath.
5. Fragments of carbon separating from the anode (in the cell or during butts cleaning) [41].
6. Carbon collar stub protection.
7. Recycled carbon from anode cover material, settled dust from offgas or butt cleaning facility [6], [44]
8. Recycled carbon in secondary alumina.

A part of these dust origins can be mitigated; however, others are inevitable due to the nature of material recycling within an aluminium smelter.

The published data on carbon particle distribution or systematic measurements of carbon content are scarce within the last 40 years. Bazhin et al. sampled RA 300 cells ranging from 0.69 to 8.19 % C, while OA-300M1 ranged from 0.71 to 5.72 % C [32]. Polakov et al. reported for similar cell technologies 0.17 to 5.09 % C [45]. Bugnion and Fischer evaluated the differences of several parameters between dusty and non-dusty cells. Dusty cells showed a carbon concentration of

0.11 % C, non-dusty cells of 0.07 % C [46]. Foosnaes et al. investigated the vertical distribution of carbon concentration for cells from Soderberg and prebaked anode technologies. A gradient was established with high concentrations close to the electrolyte surface and at the electrolyte-metal interface. However, the variation in between the sampling was larger than the overall variation of the averages per position [47].

Carbon particles have been described as dusty or fine and coarse. These different sized particles behave differently due to their density relative to the electrolyte. Coarse particles with porosity are lower in density, similar to anodes (1.45 - 1.6 g/cm^3) [47-48] and have been reported to float on top of the electrolyte, forming a foam. The smaller, fine particles are often only visible in cold electrolyte samples and are likely as dense as graphite (2.25 g/cm^3) or calcined petroleum coke (1.92 – 2.08 g/cm^3) [49]. These densities are similar to electrolyte (2.05 g/cm^3) [50-51]. A separation due to floatation would not occur. According to Foosnaes et al., the reason why certain carbon particles float on top of the electrolyte while others sink is due to variations in density [47].

1.2.3 Electrolyte Movement and Particle Distribution

Electrolyte movement can be described by two components: the dragging of electrolyte by metal movement initiated by magnetohydrodynamic (MHD) forces; and movement initiated by CO_2 bubble evolution underneath the anodes [52-53]. Further factors can be neglected in movement simulation according to Walker [54].

MHD forces describe metal velocities and the deformation of the metal-bath interface [55-56]. A faster metal movement would be associated with a higher bath drag and therefore, increases mixing. While smaller cells, like the Reynolds P19 cell design operated at TRIMET Hamburg, have two asymmetric metal circulations, larger cells like the RA300 design by RUSAL can have four or more asymmetric metal circulations [32][57]. Bilek et al. compared the effect of bath movement between CO_2 bubbles and MHD induced movement. They found the effect of bubbles far larger than the MHD effect and reflected on the dilemma with optimization of turbulence. By reducing MHD induced metal movement and CO_2 bubble evolution, the mixing of the electrolyte was reduced. This would lead to larger inhomogeneities. The use of slotted anodes can be helpful, as they mirror longer, narrow anodes that stabilize the process [58][59]. Von Kaenel et al. found slotted anodes and bubbles to have an increasing homogenization effect [60-61].

The evaluation of CO_2 bubbles and MHD effects only describe the indirect movement of particles by drag and turbulence. The description of alumina rafts is also relying on drag. An actual movement induced by an electrical field, which can be used in the process of electrophoresis, has not yet been reported for aluminium smelting, but was mentioned by Polyakov et al. [45][62].

2. Research Approach

The literature review showed three areas of interest for further research. The following paragraphs line out the areas of interest, the methods used for investigation and the relevant results.

2.1 Characterisation of Carbon Particles Found in Industrial Electrolyte

Due to the different carbon input streams, carbon particles found in the industrial electrolyte samples can give us an indication of the origin and the formation of the particles. During the study of the carbon particles varying sizes were found, which gave the impression of possibly different origins, namely from the anode and cathode. A comparison of an industrial sample with an anode and cathode samples was conducted. With the evaluation of different carbon lattice structures, one could connect the carbon particles and their respective heat treatment. The heat treatment is

considerably different between anode and cathode. Samples were taken in the Hamburg smelter operated by TRIMET Aluminium SE.

2.2 Local and Global Effects of Carbon Particles in Cells

The mechanisms for carbon dust transport within a cell are not fully understood in the published literature. From the data gathered from the analysis of industrial sampling, carbon concentrations were mapped conducted to find a common distribution pattern. The assumption was made, that carbon particles do not follow a common distribution pattern and are therefore randomly found in the electrolyte. This would be expected, as sampling in the taphole and in other positions in the cell made previously did not contain the same carbon content.

2.3 Time Dependency of Local Effects in Conjunction with Working Procedures

The literature named carbon dust and spike formation in relation to each other. The effect of the working practice quality on the anode change and spike formation were investigated in a trial series. A simple topography measurement was used to assess the area of frozen bath underneath the anode. Frozen bath from the anode's underside was sampled underneath the anodes for further investigation.

3. Methods and Experiments

In order to investigate the three questions, screening experiments and different methods were used to gain deeper insight into the effect and distribution of carbon dust. The methods are separated into Data and sample acquisition (3.1), Experimental (3.2) and Data Analysis (3.3). For the analytical methods, the analysis with STEM-EDS is presented exemplary.

3.1 Data and Sample Acquisition

3.1.1 ACD Measurement

To measure the ACD (anode cathode distance) in a cell, the distance from the anode's underside to the surface of the metal pad is measured. A metal dipstick is positioned flush underneath the anode. Due to the different freezing temperatures of electrolyte and bath, the interface is visible after 10-15 seconds and then measured with a ruler. The part submerged in metal has a thin profile compared to the part in the electrolyte.

3.1.2 Bath Sampling

A sampling tongue with a removable lid is used for bath sampling. After preheating, the tongue is submerged underneath the bath surface. There, the lid is opened and closed again via the handle. The closing mechanism prevents the sample contamination with particles floating on top of the electrolyte surface, which is important especially for cells enormous carbon dust.

3.1.3 Visual Pattern Analysis of Frozen Bath Layers

The frozen bath layers underneath freshly set anodes are measured by visual analysis. A picture of the anode from the side with a reference is taken and then mapped with a grid in MS PowerPoint. By measuring the surface and maximum height of the anode not on the hot anode, the operational safety for the campaign is improved.

3.1.4 Visual Carbon Dust Assessment

The carbon dust indexing method was published by Gudmundsson in 2011 [63]. It uses three easily distinguishable levels for different assumed carbon dust levels within a cell and is conducted during scheduled metal and bath level measurements. Level 1 has no visible carbon dust; level 2 has some carbon dust floating on top, but the amount could be removed by one scoop; level 3 has more than level 3.

3.2 Experimental

3.2.1 Short-Term Effect of Frozen Bath Underneath the Anode for Spike Formation

30 anodes were subjected to control after two, four or eight hours to measure the height of frozen bath underneath the working surface. The 30 anodes were separated into experiments with differences in relative height, work practice (cavity cleaning) and carbon dust index.

Height of newly set anode: If the newly set anode is set too high, it will not participate in the reaction for a longer period; if set too low, the heat-up can be too quick, creating thermal stress, which can lead to failure due to thermal shock, and the MHD field is disturbed [16][64-67]. Anodes in the experiments were set to their regular height or 20 mm lower.

Working quality of cavity cleaning: The use of cavity cleaning has been mentioned in literature as a counter measure for spiking and reduction of carbon dust. According to the standard operation procedure, the open anode hole has to be cleaned at least twice or until the grabber closes completely. The anodes were set according to standard or with no cavity cleaning at all.

Carbon Dust Index: Cells were distributed in two groups: little to no dust (level 1 and 2) or dusty (level 3).

The parameter combination can be found in Table 1. Anodes underneath the side risers cannot be taken out after such a short time without risking the bending or failure of the bi-clad and therefore were excluded. Earlier experiences in the smelter have shown that corner anodes were susceptible to heavy freezing and were excluded as well. Any results from middle anodes would be transferable to corner anodes, possibly even worse.

During checking of the anode, a photo was taken with a reference for further analysis (see 3.1.3). A sample was taken from underneath for further chemical and visual analysis, similar to the procedure published by Picard et al. [68-69].

3.2.2 Industrial Electrolyte Sampling and ACD Measurement Campaign

Electrolyte samples at ten positions along a cell were taken from 30 cells on two occasions (overall 60 observations at 10 positions). Bath sampling was performed as described in 3.1.2. Sampling positions can be found in Figure 2. ACD measurements were performed simultaneously according to 3.1.1.

In Figure 2, ten sampling positions (shown in circles) are equally spaced around the cell to allow access for ACD measurement underneath each anode. The grey blocks represent the anode positions. The sampling positions may vary slightly due to different side riser placement in potline 2 in Hamburg.

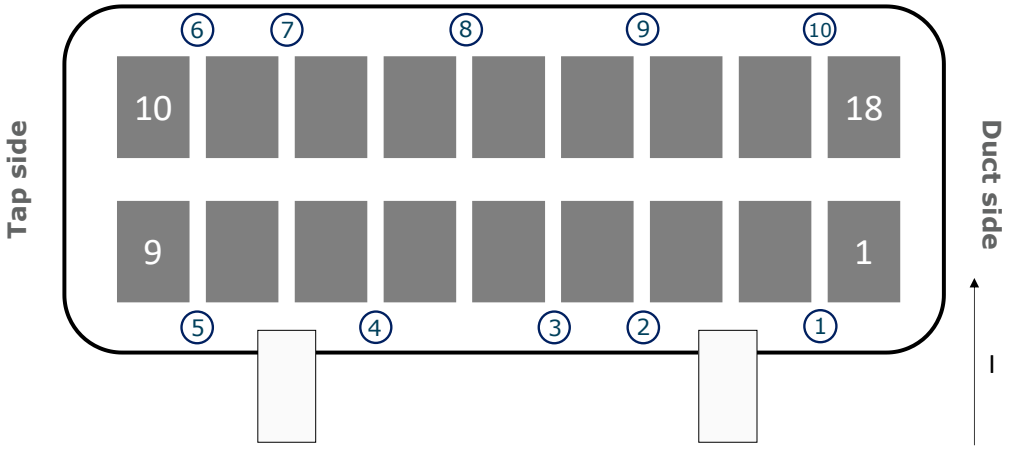

Figure 2. Bath sampling and ACD measurement positions on the cells.

3.3 Data Analysis

To establish a relation between carbon concentration found in the samples with other parameters, a PCR (Principal component regression) was applied. Other statistical tools like linear regression could not be applied due to the data available. The principal component regression uses the principle for principal component analysis (PCA), where the data is scaled and transformed linearly to a new coordinate system. The new coordinate system can describe the variation of the input data with a smaller number of variables. PCA was applied before in aluminium smelting data analysis. Tessier et al. and Majid et al. have published their analysis of process problems or anode and spike detection [70-72]. In order to reduce the risk of overfitting the model, 75 % of the data was used for model training and the rest for prediction and optimisation. The data analysis was performed with statistical language package R [73].

3.4 STEM-EDS

STEM-EDS sample preparation and analytics for the three samples (anode, cathode and electrolyte) was conducted by the Chair for Materials Chemistry at RWTH Aachen University. Scanning Transmission Electron Microscope (STEM) is a method for microscopy of thin specimens with a concentrated electron source. Samples must be able to conduct electrical current. Samples without conductivity were embedded in a silver emulsion (Leitsilber, Plano GmbH), which enables conductivity.

The specimens were prepared with the FIB (Focused Ion Beam) method, which is a precise method for thinning samples [74]. Figure 3 shows the process of thinning of samples. First, a protective layer of platinum is deposited on the sample region. Then the focused ion beam of gallium ions is used to separate the area of interest.

Afterwards, several methods of detection can be used. In this work, figures with high- angle annular dark field (HAADF) and bright field (BF) are presented. In the high-angle annular dark field of the detector zone, objects with a low density have a dark colour, while high density show a light colour. In the BF zone on the detector, the contrast is reversed.

Energy-dispersive X-Ray Spectroscopy (EDS) is a well-established method for elemental analysis, that uses an electron source to excite atoms and detects the characteristic wavelengths of elements. EDS was performed on the samples prepared as a line scan to show the distribution of elements found on the sample surface.

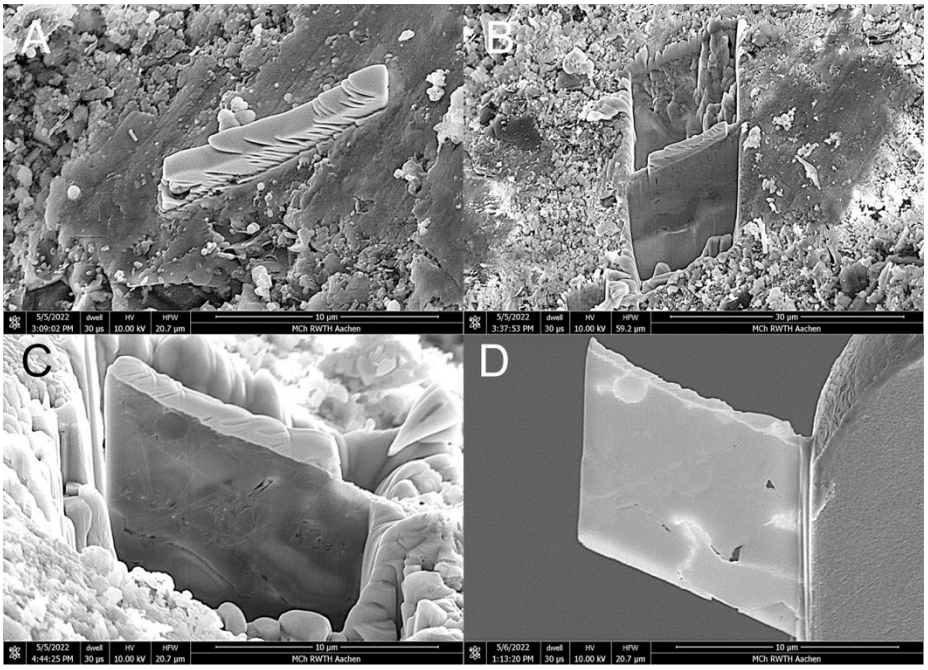

Figure 3. FIB-SEM of electrolyte sample. Process of sample extraction and thinning, showing a typical electrolyte sample; A, Platinum is deposited on the sampling area to protect the sample below; B, the sample is cut using a Gallium focused ion beam. To provide sufficient access, trenches are cut; C, the sample has been separated on the left side and will be separated further to retrieve the sample; D, sample has been retrieved and positioned on the sample holder. The final sample thickness of ~80 nm is compatible with electron microscopy.

4. Results

4.1 Frozen Bath Layer Formation

The experiments were conducted to find conditions favouring the development of a frozen bath layer. Due to the large number of variable combinations, a screening was conducted.

The estimation of frozen bath layer height was conducted as described in chapter 3.1.3. The thickness was ranging between zero cm and 15 cm. The individual combinations of the parameters and their respective maximum frozen bath layer height are shown in Table 1. The maximum heights were found for anodes, which had no proper cavity cleaning (no skimming). The shape of the frozen bath underneath the anodes suggested that pieces from the cover material of an adjacent or the former anode had fallen into the open surface and froze into the bath layer from below. This observation was made for all amounts of carbon dust. The maximum height reduced with the time since anode change. For all anodes checked eight hours after anode change the frozen bath layer was gone. The effect of skimming is significant, as a proper working procedure reduced the frozen bath height if all samples are considered as one group ($p = 0.036$). The effect was not significant after separation into the groups of non-dusty ($p = 0.173$) or dusty ($p = 0.125$) cells, as the range for the groups led to a large standard variation, especially with the results from anodes after eight hours.

Table 1. Parametrisation of frozen bath layer thickness. Odd numbers with little carbon dust (CD 1 & 2), while even numbers with high dust (CD 3). In 1 – 4 skimming was conducted as per SOP, while in 5 – 8 no skimming action was taken. 1 and 2 and 5 and 6 were set on the correct height, while 3, 4, 7 and 8 were set too low. Three scenarios were expected to behave: sp1: best case, sp2: best case with dust, sp8: worst case,

Chiffre	Skimming	Setting	Carbon Dust index	2 h	4 h	8 h
Sp1	Regular skimming	Correct height	CD 1 & 2	6	7	0
Sp2			CD 3	5	3	-
Sp3		Set too low	CD 1 & 2	6	5	0
Sp4			CD 3	5	5	-
Sp5	No skimming	Correct height	CD 1 & 2	12	15	0
Sp6			CD 3	7	10	-
Sp7		Set too low	CD 1 & 2	15	11	0
Sp8			CD 3	7	15	0

During the visual assessment of the collected bath layer samples, in a limited number of samples aluminium nuggets were found with a maximum diameter of 15 mm. The frozen bath layer had a maximum thickness of 10 cm, so the frozen part would reach at least four cm into the metal pad, assuming a six cm ACD. The droplike shape suggests the metal was captured while the bath layer was freezing.

From the 30 experiments, it was possible to collect 20 bath layer samples. From the 20 samples, 11 showed a layering behaviour (at least two layers), while nine samples included only one layer. Figure 4A shows a worst-case trial with two visible layers with an overall sampled carbon content of 1.25 % C. The upper layer (5.8 % C) includes many carbon particles with a maximum diameter of three mm. The second layer (0.224 % C) appears to be mainly cryolite/electrolyte with its white hue. Figure 4B shows a sample retrieved from best case parameter combinations. The sample shows two layers. The top layers appear porous without carbon inclusions. The lower one shows small carbon inclusions, and the porosity appears to be squeezed in the lower 15 mm. One can find small carbon particles, which would be impossible to rake out with a grabber/ pacman used in a smelter environment. The sample was analysed with 0.23 % C carbon inclusions. Figure 4C shows the visual appearance of a frozen bath composite with layers. In the mid layer one can see a layer of sintered alumina from the anode bath cover, which has dropped into the open bath surface during anode change. The frozen bath sample contains 0.036 % C. Several authors have reported the appearance of several layers, partially porous, either collected underneath the anode [68-69], as part of the crust [75-76] or in a raft formed during alumina feeding [35]. The different appearances have been attributed to cooling rates [75-76]

The effect of skimming during anode change can be shown with the sample in Figure 4D. The sample (5.48 % C) contains several carbon particles with a diameter of up to 30 mm. These particles cannot be evaluated as carbon dust, but rather broken pieces of anodes, which should be taken out during anode hole skimming.

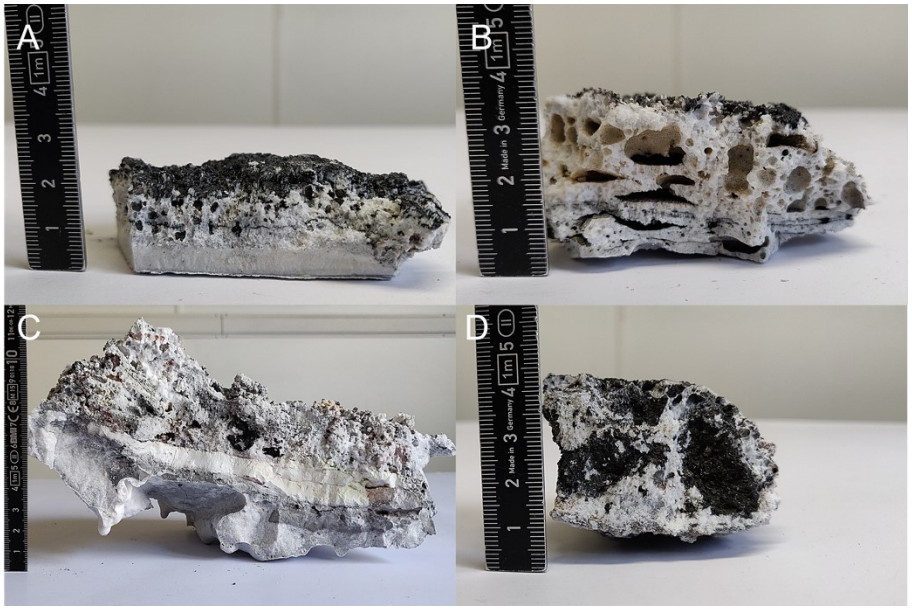

Figure 4. Frozen bath layers collected from four different experiments. The orientation of the samples is "as found" – above is the anode, below the metal ad. A: Frozen bath sample for a worst case (sp8) with two distinct layers. B: Frozen bath sample for a best-case trial (sp1) with large porosity. C: Frozen bath sample form sp7. D: Frozen bath sample from sp7 with carbon particles trapped with a maximum diameter of 30 mm.

4.2 Carbon Distribution in Cells

The distribution of carbon in the cells was analysed in two steps. At first a descriptive data analysis was conducted, then a model was created to predict future carbon concentrations. Three datasets were prepared for the analysis. Dataset 1 (ds1) includes the bath sampling data analytics, bath temperature and superheat measurement from the shift of the trial, and the sampling position (1 – 10, as visualised in Figure 2). It contains 600 rows of data. Dataset 2 (ds2) contains 1080 rows of data. Instead of the sampling position it contains the ACD measurement and the anode position (1-18). Dataset 3 (ds3) contains 60 rows of data, as it contains the averages of all data and removes the position of the sampling expect for the cell.

4.2.1 Spatial Distribution of Carbon and ACD in Cells

The carbon distribution is not normal distributed in its 600 samples. The median is at 0.085 % C, the average is considerably higher at 0.25 % C. The IQR (interquartile range between 25 % and 75 % quartiles) is 0.195 % C and the standard deviation at 0.485 % C.

The individual results from the experiments vary. Figure 5 top shows the boxplots for experiment one to 30, the plot in Figure 5 bottom for experiment 31 to 60. Experiment 1 has the lowest range from 0.022 % C to 0.059 % C, while Experiment 59 shows a range from 0.05 % C to 4.65 % C.

The distribution of carbon concentration over the sampling positions has variations. Position four (mean: 0.354 % C, median 0.148 % C), position one (mean: 0.034 % C, median: 0.109 % C) and position two (mean 0.318 % C, median: 0.124 % C) show the highest concentrations. Position two and four were located next to the side risers and therefore might experience inhomogeneous magnetic fields resulting in increased carbon dust production. Due to the large sample size in the group ($n = 600 > 30$), one can assume the Central Limit Theorem and perform Analysis of Variance (ANOVA) [77]. The results suggest that the carbon content in a measurement was more dependent on the cell it was taken from ($p = 8.08$ E-14) and not the position in the cell ($p = 0.169$).

A similar result was found for the distribution of ACD values. The ANOVA showed that the ACD is more reliant on the cell ($p < 2$ E-16) than the position in the cell ($p = 0.261$).

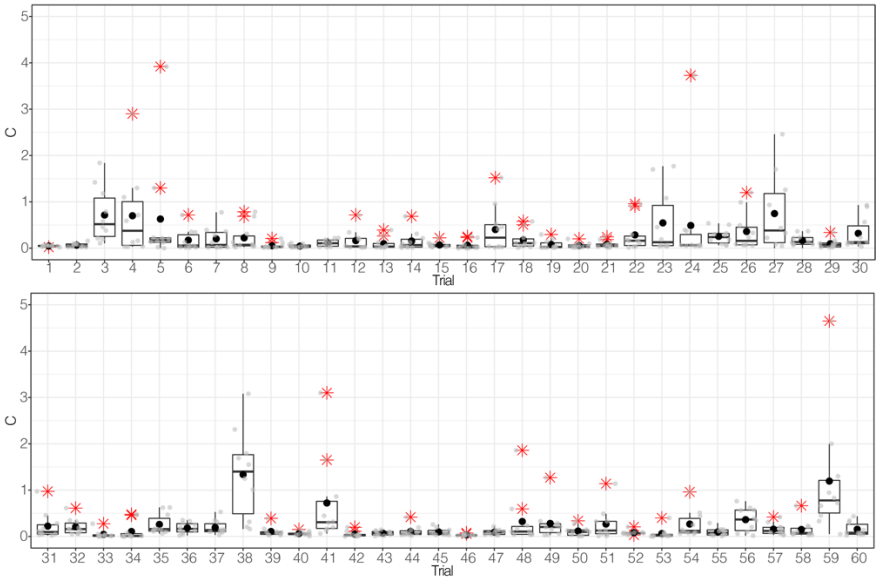

Figure 5. Carbon content distribution across 60 cells. Top: trial 1 to 30 histograms, Boxplots of carbon distribution; x-axis: trial number, y-axis: C-content in wt.-%, trials 1-30; n = 10 samples per trial; bottom: trial 31 to 60 histograms, Boxplot of carbon distribution; x-axis: trial number, y-axis: C-content in wt.-%, trials 31-60; n = 10 samples per trial.

The analysis of the measurements and sampling results shows no common pattern between position in the cell and ACD or carbon content. The variation within individual cells is smaller than the variation of spatial positions. The findings not supporting a hypothesis of common spatial patterns for ACD distribution and carbon concentration in a cell. This is in contrast to anecdotal evidence and experience of carbon dust accumulating in the corners of cells.

4.2.2 PCR Modelling – Towards a Digital Twin of Carbon Dust Production in Aluminium Electrolysis Cells

To create a model and thus eventually a digital twin for carbon dust production during aluminium electrolysis, carbon concentration within the electrolyte was modelled using the principal component regression. The three datasets described earlier were split each into 75 % data for model training and 25 % for optimisation and prediction.

For dataset ds1, the PCR model with two components can describe 69.55 % of input variance and 5.46 % of carbon concentration variance. Dataset ds2 describes 53.21 % of input variance and 3.55 % of carbon concentration variance. The model computed for dataset ds3 with one principal component can describe 19.08 % of carbon concentration variance and 39.43 % of input variance. These three models cannot explain more than 20 % of the output variance. This leads to the assumption, that the carbon concentration cannot be predicted with the collected input data as variables. The models do not account for anode and sampling position.

4.3 Origin of Carbon Dust in Aluminium Electrolysis Cell Electrolyte

Three samples (anode, cathode and electrolyte) were prepared for STEM to gain a granular insight into particles and the structures. The overview sample of the anode (see Figure 6A) shows the

anode carbon with its sponge-like texture. Sponge coke is often used for anode production and micrographs have been published [78-79]. The thinned sample shows porosity within the anode (see Figure 6B). Figure 6C shows inclusions with particle sizes between 12 and 40 nm with a higher density than carbon. The cathode sample in Figure 6D is less uniform and shows particle inclusions in the top right corner. The lower right corner has a sponge coke like appearance. Figure 6E shows the inclusions from 6D at a larger magnification. The particle sizes range from 32.38 to 768.8 nm.

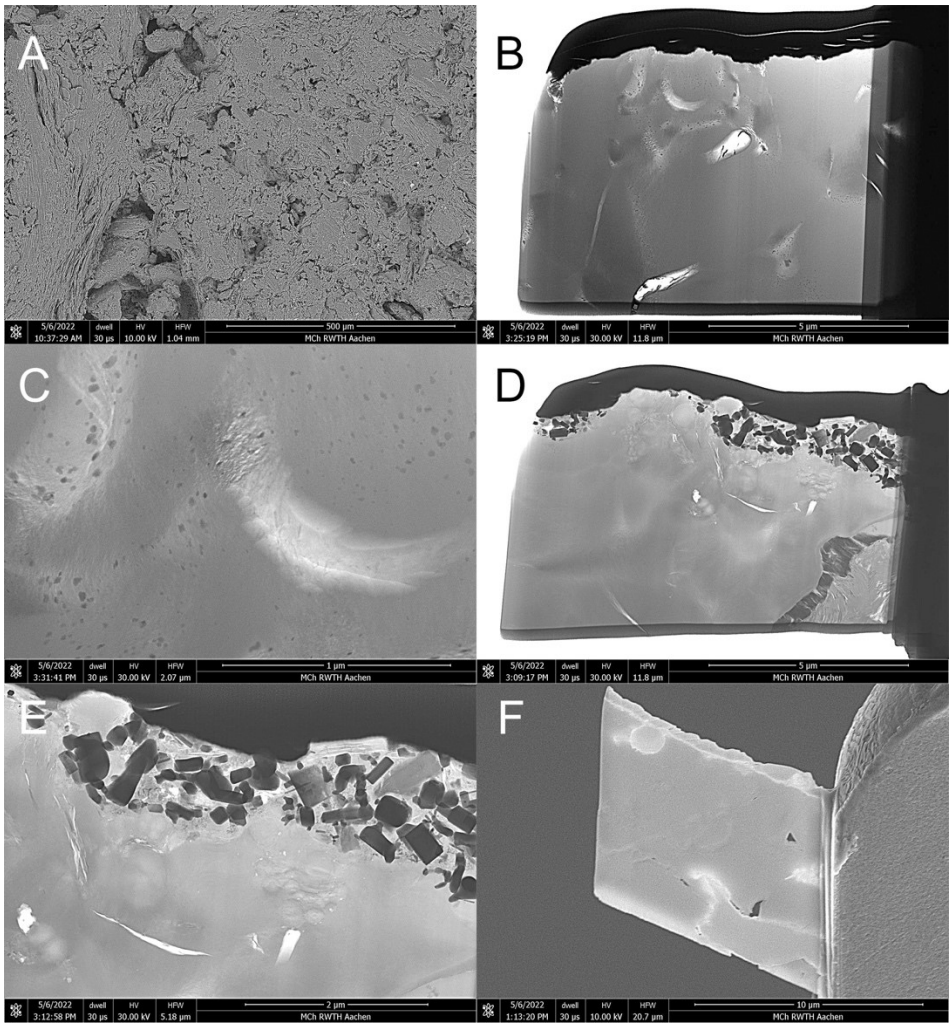

Figure 6. Electron microscopy of anode, cathode, and industrial electrolyte samples. A: SEM visualisation of anode reveals a sponge coke structure within the anode's matrix. B: STEM visualisation of the anode sample reveals large porosity in the anode structure. C: STEM of anode sample reveals micro porosity. D: STEM of cathode sample shows various interfaces of microstructures and inclusions in the top right corner. E: Higher magnification STEM showing the inclusions in the top right corner of D. F: SEM of electrolyte sample shows carbon particles in the electrolyte.

Figure 7 shows the electrolyte sample with its Al_2O_3 and carbon inclusions. The three visible carbon particles are marked with asterisks, while the alumina inclusions are marked with white arrows. The alumina particles range between 50 and 200 nm in size, while the carbon particles are significantly larger starting at 1.2 μm.

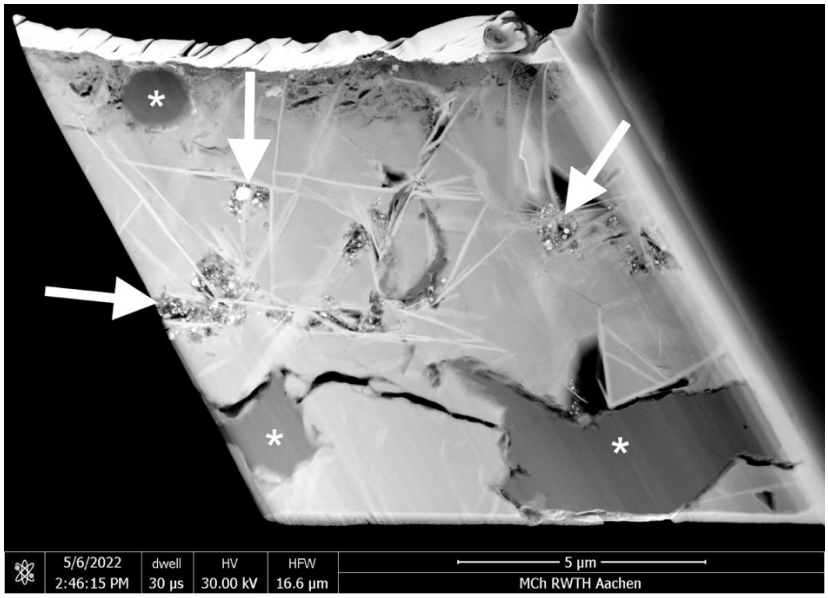

Figure 7. STEM representation of an electrolyte sample, detected by high-angle annular dark-field HAADF. High density particles are white. The sample shows dark grey carbon particles of 1.2-5 µm marked by white asterisks. Bright white alumina particles ranging from 50 to 200 nm are marked by white arrows.

Figure 8 shows the EDX line scan of the electrolyte sample revealing a cryolite matrix with carbon and alumina inclusions. Especially next to the carbon particles, sodium can be found suggesting an impregnation of carbon particles with sodium.

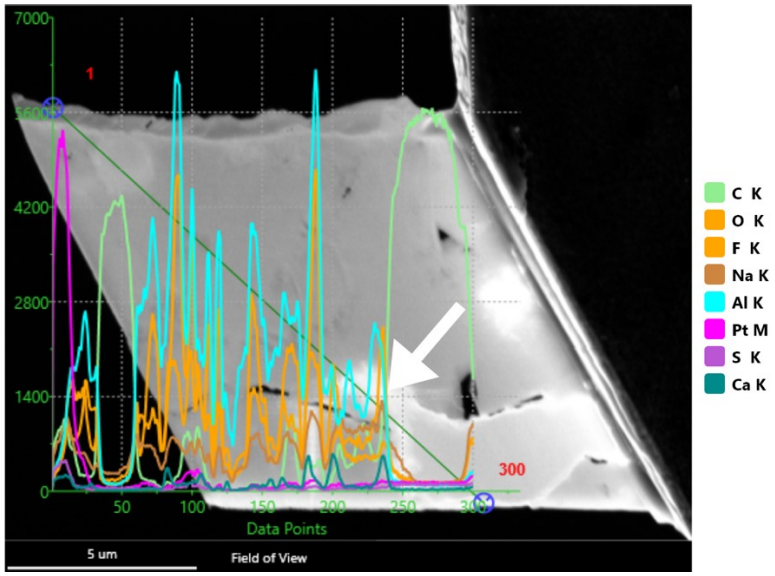

Figure 8. Line Scan EDX of an electrolyte sample. The line scan represents 300 measurements conducted in a series of traverses over the sample. The analysis shows a cryolite (Na_3AlF_6) matrix with carbon and alumina inclusions. The carbon particle on the lower right shows an increased sodium level for the first 0.85 µm suggesting sodium penetration.

The anode sample presented showed a pore structure on a nanolevel, possibly a point of reaction during air or carboxy reactivity. The pores could be the result of thermal desulphurisation [80]. The electrolyte sample showed alumina particles not yet dissolved and carbon particles embedded

within a cryolite matrix. The carbon particles appear to be impregnated on the surface by sodium. The process of sodium impregnation is well known in carbon materials [81-83]. Best practice reports suggest that carbon not participating should be removed as quickly as possible to hinder the effect of penetration, especially on recycled butts [39]. Carbon particles detaching from anodes – due to reactivity in the binder matrix - could be subjected to intercalation immediately after detachment [19].

5. Scientific Assessment

5.1 Frozen Bath Layer Formation.

The visual analysis of the frozen bath layers revealed carbon particles with diameters ranging between dust in µm or nm size and 30 mm. The formation of layers was observed. These layers could occur during different times due to cooling rates. The first layer freezes during anode insertion, while further layers freeze from further heat loss and can include pieces of sintered anode cover material [68-69]. Fine carbon particles are too small to be collected with a grabber. For that, operators have reported to use alumina powder or floor sweepings to remove floating particles. These agglomerates trap carbon and float on top of the electrolyte, like the rafts during alumina feeding [35].

Spikes are often found after three to six days according to reports published and to the author's experience [84-86]. In this study, no spikes or initial behaviour for spike formation was found and after eight hours, all frozen bath was remolten or dragged elsewhere.

5.2 Carbon Distribution in Cells

The objective of the industrial sampling was to find a distribution pattern for carbon content within the cells, as this would be in line with anecdotal evidence. A preliminary trial series suggested higher contents in corner positions and opposite of the two side risers [28].

The distribution found in the 60 cells varies. Positions right next to the side risers had the highest carbon concentration, which is in contrast with the preliminary trial series. It indicates that carbon concentration is not following a common pattern in the positions investigated. The analysis of variance (ANOVA) revealed that the carbon concentration would depend more on the cell the sample was taken form and not the position in the cell.

The data acquired were computed to find a dependency of cell parameters on the carbon concentration within the samples. The models created by principal component regression showed a low explanation of input variance (39.43 to 69.55 %) and response variable (between 3.55 % and 19.08 %) – here carbon concentration. Categorical parameters like anode position or sampling position had to be taken out due to the nature of Principal Component regression. Each expression of categorical parameter is changed to a binary variable. With the inclusion of the anode position, 18 parameters would be added. The results from the models suggest that the data acquired in the experiments cannot explain the carbon concentration variation within a cell.

5.3 Origin Analysis of Carbon Dust in Aluminium Electrolysis Electrolyte

The STEM analysis of the electrolyte showed a first visual representation of carbon in an electrolyte matrix to the best knowledge of the author The line scan chemical analysis revealed a higher concentration of sodium on the surface of carbon particles, indicating an intercalation. The intercalation is established for cathode materials [81].

The penetration of sodium into the carbon particles could be one of the explanations, why not all carbon particles float on the electrolyte surface. Capillary forces could increase the relative density and keep carbon particles floating within the electrolyte. Foosnaes et al. described the different densities in carbon particles (coke, anode or graphite) with their porosities and suggested some should float and others sink due to the relative difference in density to the electrolyte [47].

Senanu et al. investigated the electrolyte wettability of carbon materials without and with current applied. With an applied current the carbon materials showed a higher wettability and the weight of the carbon materials increased. The authors concluded that the wettability acts like a meniscus, dragging the electrodes into the electrolyte [87].

The micrographs allowed the measurement of carbon particles with diameters of 1.2 µm. These particles cannot be taken out of the cells mechanically unless they agglomerate. Therefore, one can expect to find carbon particles in industrial electrolyte samples at any time.

5.4 Mechanism of Carbon Dusting

Figure 9 shows a best- and worst-case behaviour and its influences. The pathways show the individual quality and process indicators within an anode production and the use in an electrolysis cell. The model shows the complexity of parameters within every step and is one of the reasons, why there is no easy solution to fix a dusting problem. The best-case shows no effect of the little dust produced and creates a safe work environment.

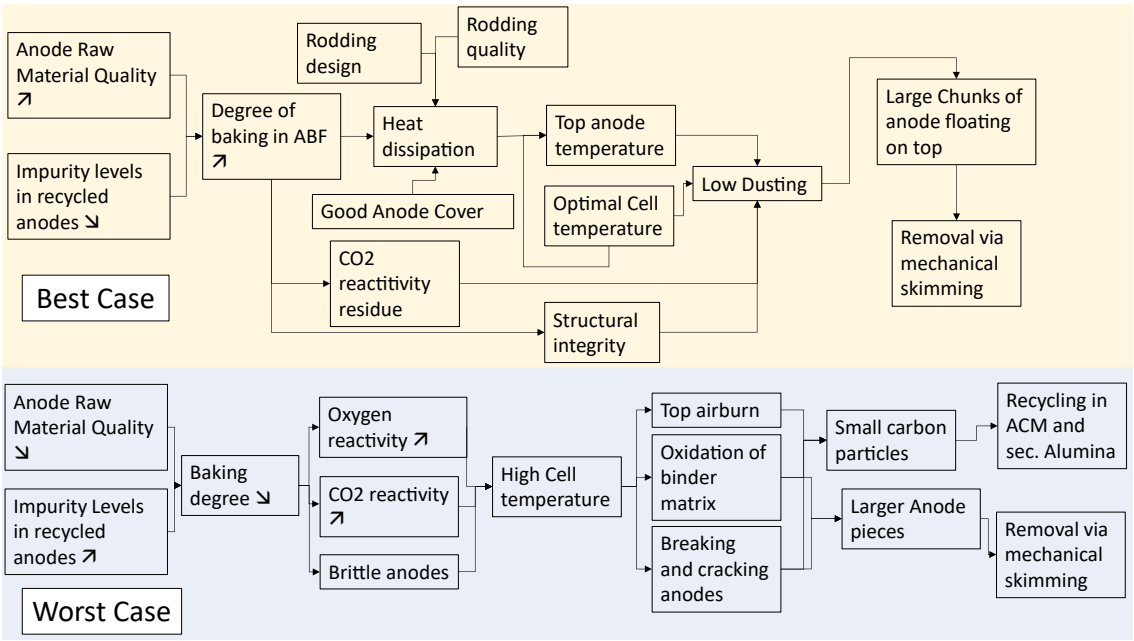

Figure 9. Mechanism of carbon dusting and carbon dust removal. Best case shown on yellow background (upper part), worst case shown on blue background (lower part).

For an improvement in the process, the options to regain control and access the best scenario track after an excursion in the worst case is often costly, but necessary. For instance, the reduction of anode rota time or use of other anodes (third party anodes) will help preventing dusting to propagate over many generations of anode cycles. To resolve a crisis on an operational level is necessary to increase the safety of workers. Procedures implied by a dusting crisis like manual skimming of carbon dust or removing broken or fallen anodes from cells are risky working procedures, even if all safety precautions are taken.

The cost of a carbon dusting crisis is estimated at 80 $ per tonne aluminium [46]. At 14 MWh per tonne, the EBITDA per tonne could calculate to 140 – 800 $ [88]. These numbers show the financial urgency to resolve a dusting crisis.

6. Summary

The presented work set out to investigate the origin and distribution of carbon particles in industrial aluminium reduction cells.

- The carbon particles found in the samples ranged from 2 µm to 30 mm, revealing the range of the problem. While larger particles can be removed with cavity cleaning, fine particles have to agglomerate before attempting removal.
- It was not possible to distinguish the origin of carbon particles (anode or cathode carbon) with the applied methods and the limited number of samples. However, it was possible to visualise carbon and alumina particles within a cryolite matrix.
- The fundamental transporting mechanism for the particles has not been found and no underlying distribution pattern could be found. The models could only explain up to 19.08 % of the variation.
- The theoretical mechanism of sodium intercalation and wettability were combined with the particle sizes found to identify particles, which float in the electrolyte or rise to the surface due to relative density.

With todays published knowledge, the use of carbon anodes will likely continue for at least 15 years, even if the inert anode research has been pushed by projects like ELYSIS or Arctus Aluminium [89-90]. Anode problems can still hinder progress and capacity creep, even in modern smelters [91-92]. Today, carbon consumption is the biggest contributor of direct carbon emissions from our industry. To fulfill prosperity and a green transition in the energy sector, demand for aluminium will only grow in the coming years [93-94].

Creating a common understanding for processes and materials instead of playing a blame game between carbon plants and electrolysis departments can help to mitigate the effects of non-optimal anodes in a smelter without heading into a crisis.

7. References

1. Uday Patel, The Outlook for the Aluminium Market in an Uncertain World, *Proceedings of the 40th International ICSOBA Conference*, 10-15 October 2022, Athens, Greece, Paper KN10, *TRAVAUX* 51, 95
2. Les Edwards *et al.*, Quantifying the Carbon Footprint of the Alouette Primary Aluminum Smelter, *JOM*, vol. 74, no. 12 Dec. 2022, 4909–4919, doi: 10.1007/s11837-022-05501-y.
3. Halvor Kvande, Gudrun Saevarsdottir, and Barry J. Welch, Direct and Indirect CO2 Equivalent Emissions from Primary Aluminium Production, *Light Metals* 2022, 998–1003, doi: 10.1007/978-3-030-92529-1_130.
4. Matthias Dechent et al., Carbon Dust—Its Short-Term Influence on Potroom Operations During Anode Change, *Light Metals* 2021, 84–392. doi: 10.1007/978-3-030-65396-5_55.
5. Louis Bugnion and Jean-Claude Fischer, "Effect of Carbon Dust on the Electrical Resistivity of Cryolite Bath, *Light Metals* 2016, 587–591. doi: 10.1007/978-3-319-48251-4_99.
6. Halldor Gudmundsson, Improving Anode Cover Material Quality at Nordural — Quality Tools and Measures, *Essential Readings in Light Metals*, 2016, 639–644, doi: 10.1007/978-3-319-48156-2_94.
7. Stanislaw Pietrzyk and Jomar Thonstad, Influence of carbon dust in the electrolyte on aluminium electrolysis parameters, *Proceedings of 33rd International ICSOBA Conference*, Dubai, UAE, 29 November–1 December 2015, *TRAVAUX* 44*, 659-666.*

8. Euel Cutshall, Influence of anode baking temperature and current density upon carbon sloughing, *Light Metals* 1986., vol. 2, 629–637.
9. V. Buzunov et al., Statistical analysis of operation of electrolyzers for aluminum production, *Tsvetnye. Metally.*, vol. 6 1994, 15–18.
10. Werner Fischer and Raymond Perruchoud, Factors Influencing the Carboxy- and Air-Reactivity Behavior of Prebaked Anodes in Hall–Heroult Cells, *Light Metals* 1986., vol. 2, 575–580.
11. N. Bird, B. McEnaney, and B. Sadler, Some Practical Consequence of Analyses of the Carboxy and Airburn Reactions of Anode Carbons, *Light Metals* 1990, 467–471.
12. Barry Sadler and S. H. Algie, Macrostructural assessment of sub-surface carboxy attack in anodes, *Light Metals* 1988, 531-540.
13. Marianne Aanvik Engvoll, Harald A. Oye, and Morten Sorlie, Gas reactivity inside industrial anodes, *Light Metals* 2002, 561–570.
14. Ioan Galasiu and Rodica Galasiu, A criterion for the classification of the quality of carbon anodes used in the aluminum electrolysis, *Revue Roumaine de Chimie*, vol. 39, no. 6 1994, 609–612.
15. D. Brooks and V. Bullough, Factors in the design of reduction cell anodes, *Light Metals* 1984, 961–976.
16. Richard W. Peterson, Temperature and Voltage Measurements in Hall Cell Anodes, in *Essential Readings in Light Metals* 2016, 500–508. doi: 10.1007/978-3-319-48200-2_67.
17. Ann Fitchett, D. Morgan, and Barry Welch, The reduction in anode airburn with protective covers, *Essential Readings in Light Metals*, 2016, 663–666.
18. Mark P. Taylor et al., The impact of anode cover control and anode assembly design on reduction cell performance, *Light Metals* 2004, 199–206.
19. Markus W. Meier, *Anodes - From the raw materials to the pot performance - Proceedings of 8th International Training Course,* 2018.
20. Hasini Wijayaratne et al., Effects of Composition and Granulometry on Thermal Conductivity of Anode Cover Materials, *Light Metals* 2011, 399–404, doi: 10.1007/978-3-319-48160-9_71.
21. Qinsong Zhang, Mark P. Taylor, and John J. J. Chen, The Melting Behaviour of Aluminium Smelter Crust, *Light Metals* 2014, 591–596, doi: 10.1007/978-3-319-48144-9_100.
22. Francois Allard, Martin Désilets, and Alexandre Blais, Thermal, chemical and microstructural characterization of anode crust formed in aluminum electrolysis cells, *Thermochimica Acta*, vol. 671 Jan. 2019, 89–102, doi: 10.1016/j.tca.2018.11.008.
23. Jérémie Lhuissier et al., Use of Under-Calcined Coke for the Production of Low Reactivity Anodes, *Essential Readings in Light Metals* 2016, 109–113, doi: 10.1007/978-3-319-48200-2_14.
24. Christopher Kuhnt et al. , Influence of Coke Calcining Level on Anode Real Density, LC and Other Properties Using a Constant Baking Cycle, *Light Metals* 2019, 1281–1289. doi: 10.1007/978-3-030-05864-7_157.
25. Gustavo Franca et al., Anode quality improvements at the Valesul smelter, in *Light Metals* 2003, 535–540.
26. Sheralyn M. Hume et al., Influence of Petroleum Coke Sulphur Content on the Sodium Sensitivity of Carbon Anodes, *Essential Readings in Light Metals*, 2016, 123–129, doi: 10.1007/978-3-319-48200-2_17.
27. Raymond Perruchoud et al., Dust generation and accumulation for changing anode quality and cell parameters, *Light Metals* 1999, 509–516.
28. Matthias Dechent, Carbon Dust Metrics for Cell and Plant Process Audits, in *Proceedings of the 39th ICSOBA Conference* 2021, Virtual Conference, Paper AL10, *TRAVAUX* 50, 727–732.
29. Aleksandr Shimanskii et al., Aluminum Smelting Carbon Dust as a Potential Raw Material for Gallium and Germanium Extraction, *JOM*, vol. 73, no. 4 2021, 1103–1109, doi: 10.1007/s11837-021-04563-8.

30. Vinko Potocnik and Michel Reverdy, History of Computer Control of Aluminum Reduction Cells, *Light Metals* 2021, 591–599, doi: 10.1007/978-3-030-65396-5_81.
31. K. R. Robilliard and Bernd Rolofs, A Demand Feed Strategy for Aluminium Electrolysis Cells, *Essential Readings in Light Metals* 2016, 747–751. doi: 10.1007/978-3-319-48156-2_111.
32. V. Yu. Bazhin et al., Concentration fields of high-power aluminum electrolyzer, *Metallurgist*, vol. 56, no. 3 2012, 284–292, doi: 10.1007/s11015-012-9572-1.
33. Pascal Lavoie and Mark P. Taylor, Alumina Concentration Gradients in Aluminium Reduction Cells, *Advances in Molten Slags, Fluxes, and Salts: Proceedings of the 10th International Conference on Molten Slags, Fluxes and Salts 2016*, 791–798, doi: 10.1007/978-3-319-48769-4_84.
34. Neal Dando et al., Impact of thermal pretreatment on alumina dissolution rate and HF evolution, *Light Metals* 2010, 541-546.
35. Sindre Engzelius Gylver et al., Alumina Feeding and Raft Formation: Raft Collection and Process Parameters, *Light Metals* 2019, 659–666. doi: 10.1007/978-3-030-05864-7_81.
36. Valdis Bojarevics and Marc Dupuis, Advanced Alumina Dissolution Modelling, *Light Metals* 2022, 339–348. doi: 10.1007/978-3-030-92529-1_47.
37. Valdis Bojarevics, In-Line Cell Position and Anode Change Effects on the Alumina Dissolution, in *Light Metals* 2021, 584–590, doi: 10.1007/978-3-030-65396-5_80.
38. Dagoberto S. Severo et al., Numerical Modeling of the Alumina Distribution in Aluar Cells, *Proceedings of the 36th International ICSOBA Conference*, Belem, Brazil, 29 October-1 November 2018, Paper AL31, *TRAVAUX* 47, 931-946.
39. Barry Sadler and Barry Welch, Reducing carbon dust?–needs and possible directions, *9th Australasian Aluminium Smelting Technology Conference and Workshops, Terrigal, Australia*, 2007
40. Kai Grjotheim, C. Krohn, and J. Thonstad, Einige offene Fragen bei der heutigen Aluminiumelektrolyse, *Internationale Leichmetalltagung* 1968, 343–346.
41. Werner K. Fischer, Felix Keller, and Raymond Perruchoud, Interdependence between anode net consumption and pot design, pot operating parameters and anode properties, *Light Metals*,1991, 681-686.
42. Abdelhalim Zoukel, Patrice Chartrand, and Gervais Soucy, Study of aluminum carbide formation in Hall-Heroult electrolytic cells, *Light Metals*, 2009, 1123–1128.
43. Henrik Gudbrandsen, A. Sterten, and R. Ødegaard, Cathodic dissolution of carbon in cryolitic melts, *Light Metals* 1992, 521–528.
44. Odd Einar Frosta, Anode Cover Material - Impact on anodes, 6th Icelandic Rodding Shop Conference, 2014.
45. P. V. Polyakov et al., On Cone Formation on Burnt Anode Face in Aluminum Electrolyzers, *Metallurgist*, vol. 60, November 9–10 2017, 1087–1093, doi: 10.1007/s11015-017-0411-2.
46. Louis Bugnion and Jean-Claude Fischer, Carbon dust in aluminium electrolysis pots–a vicious circle, *Proceedings of the 33rd International ICSOBA Conference*, Dubai, UAE, 29 November-1 December 2015, Paper AL16, *TRAVAUX* 44, 649-657.
47. T. Foosnaes et al., Anode Dusting in Hall–Heroult Cells, *Light Metals* 1986., vol. 2, 729–738.
48. Markus Meier, Raymond Perruchoud, and Julien Wyss, Bench mark prebaked anode production with russian raw materials, *Журнал Сибирского федерального университета. Техника и технологии*, vol. 9, no. 5 2016, 731–743.
49. Les Edwards et al., Use of Shot Coke as an Anode Raw Material, in *Essential Readings in Light Metals* 2016, 36–41, doi: 10.1007/978-3-319-48200-2_6.
50. Halvor Kvande and H. Roervik, The influence of bath density in aluminium electrolysis, *Light Metals* 1985, 671–678.
51. Warren Haupin, The influence of additives on Hall-Héroult bath properties, *JOM*, vol. 43, no. 11 1991, 28–34, doi: 10.1007/BF03222717.

52. Jayson Tessier, Katie Cantin, and David Thor Magnusson, Investigation of alumina concentration gradients within Hall-Héroult electrolytic bath, *Light Metals* 2018, 515–522.
53. Kristian Etienne Einarsrud et al., Towards a coupled multi-scale, multi-physics simulation framework for aluminium electrolysis, *Applied Mathematical Modelling*, vol. 44, Apr. 2017, 3-24, doi: 10.1016/j.apm.2016.11.011.
54. Marcus L. Walker, *Fluid dynamic phenomena in aluminium production processes*, Ph.D. thesis, University of Auckland, Auckland, New Zealand, 1995.
55. Hendrik Gesell and Uwe Janoske, Magnetohydrodynamic Analysis of Load Shifting in Hall-Heroult Cell, *Proceedings of the 40th International ICSOBA Conference*, 10-15 October 2022, Athens, Greece, Paper AL19, *TRAVAUX* 51, 1235–1246.
56. Michel Reverdy and Vinko Potocnik, History of Inventions and Innovations for Aluminum Production, *TMS 2020 149th Annual Meeting & Exhibition Supplemental Proceedings*, The Minerals, Metals & Materials Society, 1895–1910, doi: 10.1007/978-3-030-36296-6_175.
57. D. Vogelsang, Application of Integrated Simulation Tools for Retrofitting Aluminium Smelters, *4th Australasian Aluminium Smelter Techn. Workshop*, 1992, pp. 25–30.
58. M. M. Bilek, W. D. Zhang, and F. J. Stevens, Modelling of electrolyte flow and its related transport processes in aluminium reduction cells, *Light Metals* 1994, 323–323.
59. Dagoberto S. Severo et al., Modeling the Bubble Driven Flow in the Electrolyte as a Tool for Slotted Anode Design Improvement, in *Essential Readings in Light Metals*, 2016, 409–414. doi: 10.1007/978-3-319-48156-2_58.
60. René von Kaenel et al., Magnetohydrodynamic and bubbles driving forces impact on dispersion and convection of alumina in the bath of an Hall-Héroult cell, 5th International Congress & Exhibition Non-ferrous Metal, Krasnoyarsk, Russia, 2013.
61. René von Kaenel et al., Impact of magnetohydrodynamic and bubbles driving forces on the alumina concentration in the bath of an Hall-Héroult cell, *Light Metals* 2013, 585–590. doi: 10.1007/978-3-319-65136-1_100.
62. Ryan T. Turgeon and Michael T. Bowser, Micro free-flow electrophoresis: theory and applications, *Analytical and bioanalytical chemistry*, vol. 394, no. 1 2009, 187–198, doi: 10.1007/s00216-009-2656-5.
63. Halldor Gudmundsson, Anode Dusting from a Potroom Perspective at Nordural and Correlation with Anode Properties, *Light Metals* 2011, 471–476.
64. Frank Aune et al., Thermal effects by anode changing in prebake reduction cells, *Light Metals* 1996, 429-436.
65. Jacques Antille and René von Kaenel, Using a Magnetohydrodynamic Model to Analyze Pot Stability in Order to Identify an Abnormal Operating Condition, *Essential Readings in Light Metals*, 2016, 367–372. doi: 10.1007/978-3-319-48156-2_52.
66. Marianne Jensen et al., ACD measurement and theory, *Light Metals* 2009, 455–459.
67. Vanderlei Gusberti et al., Modeling the effect of the anode change sequence with a non-linear shallow water stability model, *Light Metals* 2007, 157–164.
68. Donald Picard et al., Investigation of the Frozen Bath Layer under Cold Anodes, *Metals*, vol. 7, no. 9, Sep. 2017, 374, doi: 10.3390/met7090374.
69. Donald Picard et al., In Situ Evolution of the Frozen Layer Under Cold Anode, *Light Metals* 2019, 795–802. doi: 10.1007/978-3-030-05864-7_97.
70. Nazatul Aini Abd Majid et al., Aluminium process fault detection by Multiway Principal Component Analysis, *Control Engineering Practice*, vol. 19, no. 4 Apr. 2011, 367–379, doi: 10.1016/j.conengprac.2010.12.005.
71. Nazatul Aini Abd Majid et al., Multivariate statistical monitoring of the aluminium smelting process, *Computers & Chemical Engineering*, vol. 35, no. 11 Nov. 2011, 2457–2468, doi: 10.1016/j.compchemeng.2011.03.001.
72. Jayson Tessier et al., Analysis of a potroom performance drift, from a multivariate point of view," *Light Metals*, 2008, 319-324.
73. R Core Team, R: A Language and Environment for Statistical Computing. Vienna, Austria: R Foundation for Statistical Computing, 2022. Available: https://www.R-project.org/

74. B. Nagamani Jaya et al., Non-conventional Small-Scale Mechanical Testing of Materials, *J Indian Inst Sci*, vol. 102, no. 1 Jan 2022, 139–171, doi: 10.1007/s41745-022-00302-3.
75. Sándor Poncsák et al., Impact of the Solidification Rate on the Chemical Composition of Frozen Cryolite Bath, *Metals*, vol. 7, no. 3 2017, 97, doi: 10.3390/met7030097.
76. Sándor Poncsák et al., Impact of the Heat Flux on Solidification of Cryolite Based Bath, *Light Metals* 2016, 359–364. doi: 10.1007/978-3-319-48251-4_59.
77. Xijuan Zhang et al., How to think clearly about the central limit theorem, *Psychological Methods*, Mar. 2022, doi: 10.1037/met0000448.
78. Keith Neyrey et al., A tool for predicting anode performance of non-traditional calcined cokes, *Light Metals* 2005, 607–612.
79. Les Edwards, The history and future challenges of calcined petroleum coke production and use in aluminum smelting, *JOM*, vol. 67, no. 2 2015, 308–321, doi: 10.1007/s11837-014-1248-9.
80. Les Edwards, Kevin Harp, and Christopher Kuhnt, Use of Thermally Desulfurized Shaft CPC for Anode Production, *Light Metals* 2017, 1173–1181.
81. Kati Tschöpe, *Degradation of Cathode Lining in Hall-Héroult Cells*, PhD Thesis, Norwegian University of Science and Technology, Trondheim, Norway, 2010.
82. Pierre-Yves Brisson et al., Revisiting sodium and bath penetration in the carbon lining of aluminum electrolysis cell, *Light Metals* 2005, 727–732.
83. Hanns-Peter Boehm, Ralph Setton, and Eberhard Stumpp, Nomenclature and terminology of graphite intercalation compounds (IUPAC Recommendations 1994), *Pure and Applied Chemistry*, vol. 66, no. 9, pp. 1893–1901, Jan. 1994, doi: 10.1351/pac199466091893.
84. Matthias Dechent, An Anode Crisis - The Pitfalls of an Anode Length Increase, *Proceedings of the 41st International ICSOBA Conference*, 5-9 November 2023, Dubai, UAE, Paper AL17, *TRAVAUX* 52, 1375–1385.
85. M. Ali and A. Omran, Anode spike formation in prebaked aluminium reduction cells, *JAUES*, vol. 7, no. 4, pp. 29–40, 2012.
86. Bernd Rolofs and Neal Wai-Poi, The effect of anode spike formation on operational performance, *Light Metals*, 189–193, 2000.
87. Samuel Senanu et al., Wetting of Carbon Cathodes by Molten Electrolyte and Aluminium, *Light Metals* 2021, 699–707. doi: 10.1007/978-3-030-65396-5_92.
88. Martin Iffert, The Decarbonisation Journey of the Aluminium Industry - Opportunities and Challenges to Achieve Net-Zero, *Proceedings of the 41st International ICSOBA Conference*, 5-9 November 2023, Dubai, UAE, Paper KN02, *TRAVAUX* 52, 47-66.
89. Halvor Kvande, Net-Zero emissions from Primary Aluminium Production - Is this technologically and economically possible?, *Proceedings of the 41st International ICSOBA Conference*, 5-9 November 2023, Dubai, UAE, Paper KN03, *TRAVAUX* 52, 67-76.
90. N. N, CO2-freie Aluminiumproduktion, *TRIMET Aluminium SE*, https://www.trimet.eu/de/trimet/nachhaltigkeit/umwelt-und-klimaschutz/herstellung-von-inerten-metallischen-anoden (Accessed on Nov. 18, 2023).
91. Anthony Di Paola and Matthew Martin, Maaden Aluminum Smelter Cut Production on Operating Issues, *Bloomberg.com,* https://www.bloomberg.com/news/articles/2023-01-11/maaden-aluminum-smelter-cut-production-after-operating-problems (Accessed on Nov. 18, 2023).
92. Ishaq Alkharusi and Vishal Ahmad, Amperage Increase in EGA Al Taweelah DX Technology Potlines, *Proceedings of the 41st International ICSOBA Conference*, 5-9 November 2023, Dubai, UAE, Paper AL01, *TRAVAUX* 52, 1209–1219.
93. Dierk Raabe, The Materials Science behind Sustainable Metals and Alloys, *Chem. Rev.*, vol. 123, no. 5, 2436–2608, Mar. 2023, doi: 10.1021/acs.chemrev.2c00799.
94. Sunil Gupta and Nitin Kumar Tiwari, "Future of Indian Aluminium Sector: Challenges and Progress *Proceedings of the 41st International ICSOBA Conference*, 5-9 November 2023, Dubai, UAE, Paper KN07, *TRAVAUX* 52, 119–126.